



Detection of electron showers in dual-readout crystal calorimeters

N. Akchurin^a, F. Bedeschi^b, A. Cardini^c, M. Cascella^{d,b}, G. Ciapetti^{e,f}, A. d'Orazio^{e,f}, L. Collica^{g,h,1}, D. De Pedis^f, R. Ferrari^g, S. Franchino^{g,h,1}, M. Fraternali^{g,h}, G. Gaudio^g, P. Genova^{g,h}, J. Hauptmanⁱ, F. Lacava^{e,f}, L. La Rotonda^{j,k}, S. Lee^a, M. Livan^{g,h}, E. Meoni^l, A. Negri^{g,h}, D. Pinci^f, A. Policicchio^{j,k}, F. Scuri^b, A. Sill^a, T. Venturelli^{j,k}, C. Voena^f, R. Wigmans^{a,*}

^a Texas Tech University, Lubbock, TX, USA

^b INFN Sezione di Pisa, Italy

^c INFN Sezione di Cagliari, Monserrato, CA, Italy

^d Dipartimento di Fisica, Università di Pisa, Italy

^e Dipartimento di Fisica, Sapienza Università di Roma, Italy

^f INFN Sezione di Roma, Italy

^g INFN Sezione di Pavia, Italy

^h Dipartimento di Fisica Nucleare e Teorica, Università di Pavia, Italy

ⁱ Iowa State University, Ames, IA, USA

^j Dipartimento di Fisica, Università della Calabria, Italy

^k INFN Cosenza, Italy

^l Institut de Física d'Altes Energies (IFAE), Universitat Autònoma de Barcelona, Bellaterra, Barcelona, Spain

ARTICLE INFO

Article history:

Received 7 February 2012

Received in revised form

12 April 2012

Accepted 13 April 2012

Available online 2 June 2012

Keywords:

Calorimetry

Čerenkov light

High-Z scintillating crystals

ABSTRACT

Some high-Z scintillating crystals offer the possibility to distinguish the contributions from the scintillation and Čerenkov mechanisms to the generated signals. Among these crystals are BGO and PbWO₄. We have tested matrices of these crystals as electromagnetic calorimeters and studied the properties of the Čerenkov and scintillation components of the signals generated by high-energy electrons showering in these detectors.

© 2012 Elsevier B.V. All rights reserved.

1. Introduction

Dual-readout calorimetry was proposed as a technique that would make it possible to eliminate the factors that traditionally limit and spoil the performance of the large hadron calorimeters operating in modern particle physics experiments at the energy frontier. By comparing the signals generated in the form of Čerenkov and scintillation light, it is possible to determine the electromagnetic shower fraction for individual events. Event-by-event fluctuations in this fraction (f_{em}) are the main culprit for the problems encountered in hadron calorimetry. Experimental tests with the DREAM calorimeter have clearly demonstrated the validity of this principle [1].

The DREAM calorimeter consisted of a copper absorber structure into which thousands of optical fibers were embedded. Scintillating fibers detected the scintillation light, whereas the

Čerenkov light was generated in clear (undoped) fibers. However, there is no fundamental reason why a dual-readout calorimeter ought to be equipped with two independent active media. In particular, one could use the signals generated by high-energy showers in crystals, provided that these signals can be decomposed into scintillation and Čerenkov components. Using crystals as dual-readout calorimeters offers potential benefits, since one could then in principle eliminate or greatly reduce two remaining sources of fluctuations that dominated the hadronic resolution of the fiber calorimeter, namely *sampling fluctuations* and *fluctuations in the Čerenkov light yield*.

In recent years, we have developed four different methods to split crystal signals into their scintillation and Čerenkov components [2–5,7,8]. These methods exploit

1. differences in the angular distribution of the light [2],
2. differences in the spectral characteristics [3],
3. differences in the time structure of the signals [3], and
4. the fact that Čerenkov light is polarized, while scintillation light is not [7].

* Corresponding author. Fax: +1 806 742 1182.

E-mail addresses: Richard.Wigmans@ttu.edu, wigmans@ttu.edu (R. Wigmans).

¹ Now at Department of Physics and INFN, University of Milano Statale, Italy.

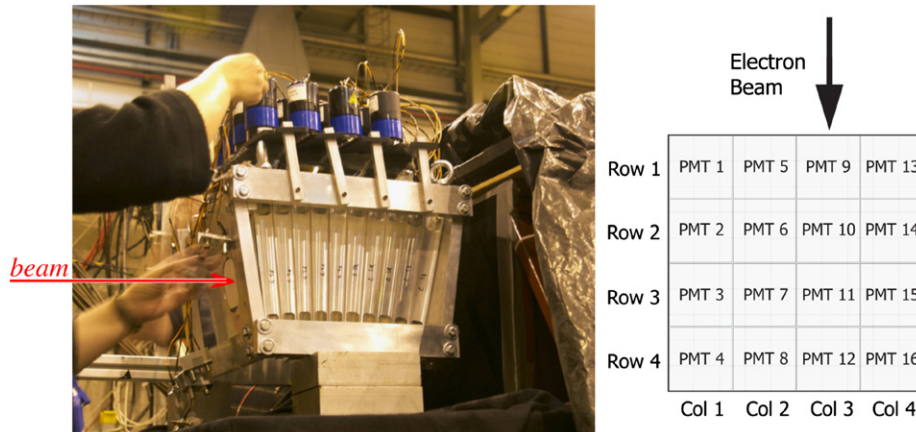


Fig. 1. The BGO matrix consisted of 100 tapered crystals. They were read out from the top by 16 PMTs, each of which was equipped with a UG11 filter (see Table 1), while the beam entered from the side, as shown. The accompanying diagram shows the arrangement of the PMTs in rows and columns, as well as the PMT numbering.

These methods were experimentally investigated and optimized for three different types of crystals: bismuth germanate (BGO) [3], bismuth silicate (BSO) [8] and lead tungstate (PbWO_4) [2,3]. The latter crystal was also doped with small amounts of impurities to further improve its dual-readout characteristics [4,5].

All these studies were carried out with high-energy muons, pions or electrons that traversed a single crystal. In this paper, we investigate to what extent the promise of improved calorimeter performance can be realized with such crystals. The reduced contributions of sampling fluctuations and fluctuations in the Čerenkov light yield would first and foremost manifest themselves in the performance for *electromagnetic* shower detection, since such fluctuations dominate the em energy resolution. We constructed two crystal matrices that were large enough to contain high-energy electron showers. One matrix consisted of 100 BGO crystals used previously in the L3 experiment [9], the other one consisted of 7 custom made PbWO_4 crystals doped with 0.3% molybdenum. These detectors were instrumented in such a way that both scintillation and Čerenkov signals could be extracted from the light produced by showering particles. They were tested in electron beams with energies ranging from 4 to 180 GeV in the H8 beam of the CERN Super Proton Synchrotron, in the context of CERN's recently approved RD52 program.

In Section 2, the detectors and the experimental setup in which they were tested are described, as well as the calibration and data analysis methods that were used. Experimental results are presented in Section 3. In Section 4, we discuss the implications of these results.

2. Equipment and measurements

2.1. The crystal matrices

Calorimeters consisting of high-Z scintillating crystals are the detectors of choice in particle physics experiments that aim for the best energy resolution in electron and γ detection. Examples of recent experiments using such calorimeters include BaBar at SLAC [10], Belle at KEK [11], L3 at LEP [9] and CMS at the LHC [12]. However, our goals are different from those in the mentioned experiments, in the sense that we want to use crystals for dual-readout purposes, in order to achieve superior *hadronic* calorimeter performance. The question is then if and to what extent crystals optimized for this purpose can at the same time also be excellent em calorimeters.

Of the four methods that we developed to separate the light signals generated in the crystals into scintillation and Čerenkov components (see Section 1), only numbers two (spectral differences) and three (time structure) are easily applicable in the hermetic detectors needed for 4π experiments at colliding beams. The two matrices built for our purpose are based on these methods, in which filters are used to select (or at least strongly enhance the relative abundance of) the desired type of light, and the time structure provides a powerful tool to distinguish between the contributions of the (prompt) Čerenkov and (delayed) scintillation components to the detected signals. Since the intensity of the unfiltered light is completely dominated by the scintillation component, and since obtaining pure signals of the two individual components works best when their intensities are comparable to begin with Ref. [13], the purpose of filtering is primarily to reduce the intensity of the scintillation component. For example, in the case of BGO, the chosen filtering reduces the strength of this component by three orders of magnitude. As a result, the remaining light yield is such that fluctuations in the detected numbers of photoelectrons become a significant contribution to the em energy resolution. This is an important difference with experiments in which the unfiltered light of such crystals is used for the em calorimeter signals. In any case, since the detection of Čerenkov light is *the* crucial issue for the dual-readout method, our primary interest in the present study is the precision with which the calorimeter performance can be measured using this signal component.

2.1.1. The BGO matrix

The first matrix consisted of 100 crystals of bismuth germanate ($\text{Bi}_4\text{Ge}_3\text{O}_{12}$). The crystals were 24 cm long and tapered. One end face had a cross-section of $2.4 \times 2.4 \text{ cm}^2$, the other one measured $3.2 \times 3.2 \text{ cm}^2$. These crystals formed a projective segment from the L3 calorimeter. This segment was placed perpendicular to the beam line, as shown in Fig. 1. For electrons entering the matrix in its geometrical center, it had an effective thickness of 28 cm, i.e. 25 radiation lengths (X_0).

For the purpose of these tests, this ensemble of crystals was considered one unit. The detector was read out by 16 square PMTs,² each with a photocathode surface of $7.6 \times 7.6 \text{ cm}^2$. The readout arrangement of the PMTs, shown in the right diagram of

² Photonis XP3392B, 8-stage, bi-alkali photocathode, nominal gain 2.3×10^5 at 1000 V.

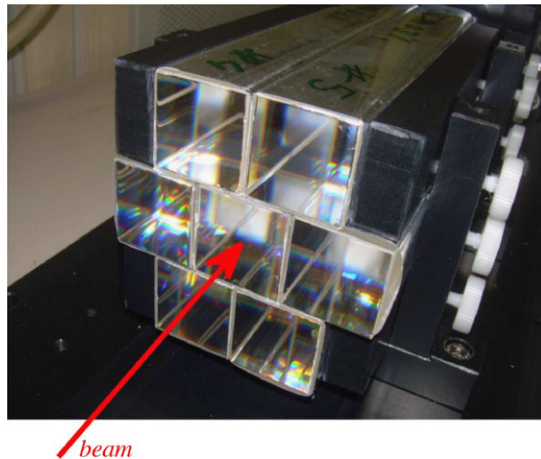


Fig. 2. The PWO matrix consisted of seven crystals with dimensions of $3 \times 3 \times 20$ cm³. These were arranged as shown in the figure and the beam entered the matrix in the central crystal. All crystals were individually wrapped in aluminized mylar. Both the upstream and downstream end faces were covered with filters. See text for details.

Fig. 1, was such that each PMT collected light produced by clusters of at least 9 adjacent crystals.

In order to increase the Čerenkov/scintillation ratio to the point that useful Čerenkov signals could be obtained, we used UG11 filters (see Table 1). These UV filters were also successfully used for this purpose in previous studies [3,8]. Each PMT had its own filter.

2.1.2. The PbWO₄ matrix

The PbWO₄ matrix consisted of seven crystals with dimensions of $3 \times 3 \times 20$ cm³. These crystals were specifically produced according to our specifications, by the Radiation Instruments and New Components company in Minsk (Belarus). They were doped with 0.3% molybdenum, which had two important effects [4,5]:

- The emission spectrum of the PbWO₄ crystals was shifted to somewhat longer wavelengths.
- The decay time of the scintillation process increased from ~ 10 ns to ~ 25 ns.

Both effects made it considerably easier to extract the Čerenkov component from the light produced by these crystals, and to increase the purity of the Čerenkov and scintillation signals.

Before the matrix was assembled, all crystals were individually tested in a high-energy particle beam. These tests served to determine their light yield and attenuation characteristics.

After that, they were arranged in a matrix as shown in Fig. 2 and placed in the beam line. The beam entered this matrix in the central crystal. The longitudinal dimension, relevant for our measurements, corresponded to 22.5 radiation lengths (X_0). Transversely, the total width of three crystals corresponded to 4.5 Moliere radii. The light produced by electrons showering in this matrix was read out by photomultiplier tubes (PMTs) located at opposite ends (two for each crystal, 14 PMTs in total). We used Hamamatsu R8900-100 tubes for this purpose.³ Both the upstream and downstream end faces of the matrix were covered with a large optical transmission filter. In order to provide good optical contact between the crystal surface, the filter and the PMT

³ 10-Stage, effective photocathode area 25×25 mm², super bi-alkali photocathode.

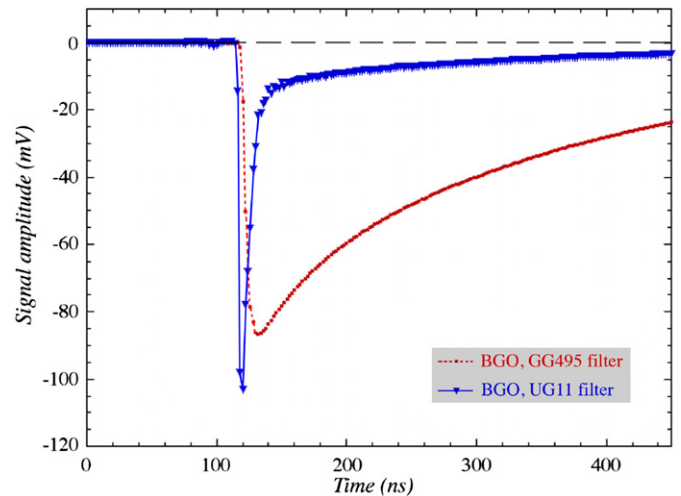


Fig. 3. The time structure of typical signals measured in a single BGO crystal, placed perpendicular to the beam line. The crystal was equipped on one side with a yellow filter, and on the other side with a UV filter, and read out with small, fast PMTs. The signals were measured with the sampling oscilloscope at a rate of 0.5 GHz, or 2.0 ns per sample.

window, and thus reduce the light trapping effects of the large refractive index of PbWO₄ ($n=2.2$), we used Elastosil (silicone) “cookies”, which had an index of refraction $n=1.403$. Several filter combinations were used during our experiments. These are discussed in the next subsection.

2.1.3. The filters

The importance of optical transmission filters for our purpose was first demonstrated with BGO [3]. Fig. 3 shows the typical signal shapes for events in which beam particles traversed a single crystal placed perpendicular to the beam line. One side of the crystal was equipped with a yellow transmission filter, the other side with a filter that only transmitted light with wavelengths shorter than 400 nm.

The signals were read out with small, fast PMTs⁴ in these measurements.

The UV filter absorbed $>99\%$ of the scintillation light [3], while a large fraction of the Čerenkov light, which exhibits a λ^{-2} spectrum [14], was transmitted. As a result, the Čerenkov component of the light produced by the crystal became clearly visible, in the form of a prompt peak superimposed on the remnants of the scintillation component, which has a decay time of ~ 300 ns. The UG11 filters were used for all BGO measurements described in this paper.

The effects of using these filters were even more spectacular in the case of the molybdenum-doped PbWO₄ crystals. Fig. 4 shows that a measurement similar to that described above for BGO led to a more or less complete separation of the Čerenkov and scintillation components.

Yet, UG11 was less suitable for the PbWO₄ signals, because of the strong self absorption of short-wavelength light in these crystals. This is illustrated in Fig. 5b, which shows that the absorption coefficient strongly increases for $\lambda < 380$ nm. As a result, Čerenkov signals obtained with this filter were rather small and strongly depended on the distance the light had to travel to the PMT [4]. For these reasons, in the present study other UV filters were chosen to separate the Čerenkov and scintillation components, in particular U330 and UG5 (see Table 1).

⁴ Hamamatsu R1355, square (28 mm), 10-stage, 25×25 mm² bi-alkali photocathode.

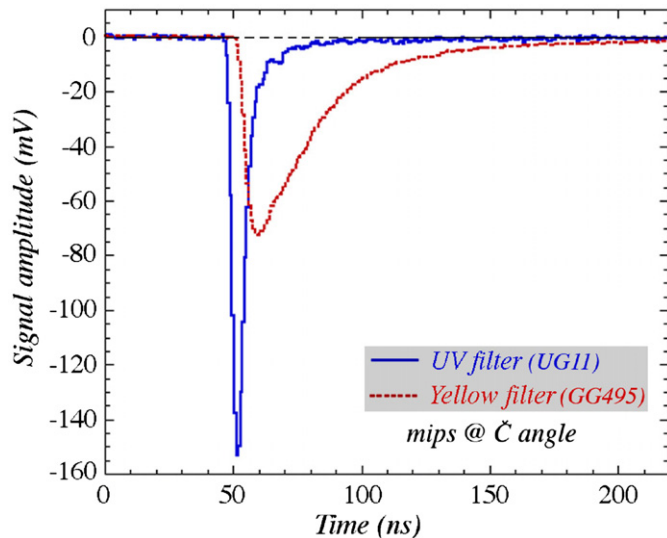


Fig. 4. Average time structure of the signals from a single Mo-doped PbWO_4 crystal, placed at an angle of 60° with the beam line. The light produced by the particles traversing this crystal was filtered with UG11 and GG495 filters, respectively.

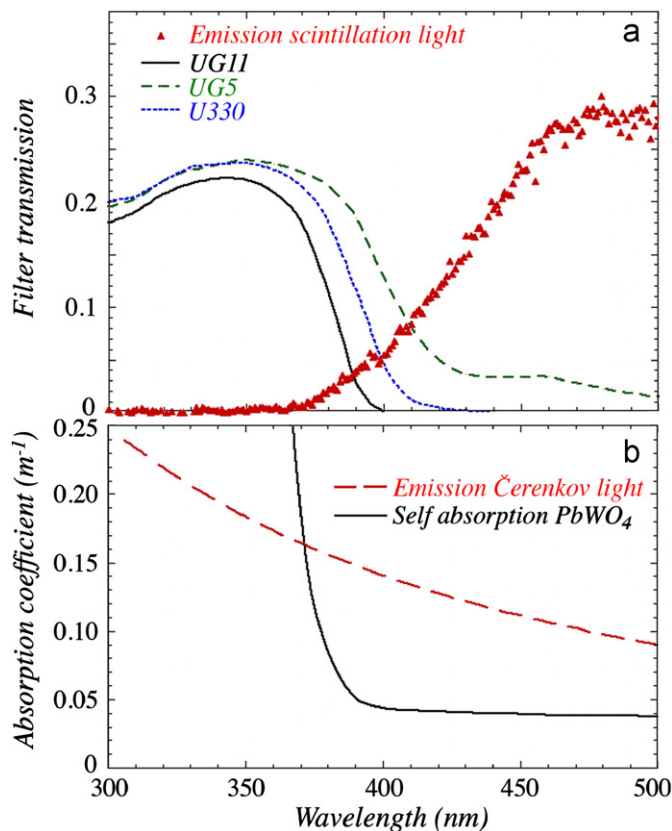


Fig. 5. Emission and absorption characteristics relevant to the PbWO_4 crystal matrix. Diagram (a) shows the emission spectrum of the scintillation light, as well as the transmission characteristics of three filters used to obtain the Čerenkov signals. In diagram (b), the Čerenkov spectrum is plotted, together with the self-absorption coefficient of the PbWO_4 crystals, as a function of the wavelength [5].

The transmission curves of all mentioned UV filters are shown in Fig. 5a, together with the spectrum of the scintillation light emitted by the Mo-doped PbWO_4 crystals. The U330, and especially the UG5 filter transmitted a significant fraction of the scintillation light. However, the extension to longer wavelengths

Table 1

Properties of the different optical transmission filters that were used in the studies of the doped PbWO_4 crystals. All filters were 3 mm thick and made of glass. The U330 filter was made by Hoya, the other ones by Schott. See Fig. 5a for transmission curves.

Filter type	Filter name	> 90% transmission for (nm)
UG11	“UV”	$\lambda < 400$
U330		$\lambda < 410$
UG5	“Blue”	$\lambda < 460$
GG495	“Yellow”	$\lambda > 495$

also meant that a larger fraction of the Čerenkov light contributed to the signals (Fig. 5b). In addition, the detected Čerenkov light was less attenuated than with the UG11 filter.

For the measurements described in this paper, the PbWO_4 matrix was equipped with filters both at the upstream and downstream end faces of the crystals. We report on the following configurations:

1. Upstream GG495, downstream U330.
2. Upstream U330, downstream U330.
3. Upstream U330, downstream UG5.

2.2. The beam line

All measurements described in this paper were carried out in the H8 beam line at CERN’s Super Proton Synchrotron. The electron beams were produced in one of two ways

1. As secondary beams produced by the 400 GeV primary proton beam. The secondary particles were momentum selected, and hadron/electron separation was achieved by making use of the fact that the electrons emit much more synchrotron radiation when being bend in a magnetic dipole field. A 180 GeV beam of this type was used in our experiments.
2. Tertiary beams, in which the secondary beam particles are sent through a $1X_0$ radiator (5 mm lead). Contrary to the pions, electrons in this beam lose a significant fraction of their energy in this process and the downstream beam optics are tuned to select these lower-momentum electrons.

Using these two methods, we could obtain rather pure electron beams with momenta ranging from 4 to 180 GeV/c. However, the rates for tertiary beams were very low and therefore the collimators had to be opened to the point that the momentum bite of the selected beam particles was not entirely negligible. Based on available documentation [6], we estimated $\Delta p/p$ to be of the order of 1.5%.

The experimental setup is schematically (and *not* to scale) shown in Fig. 6. Two small scintillation counters ($T1$, $T2$) and a veto counter provided the signals that were used to trigger the data acquisition system. The counters $T1$ and $T2$ were 2.5 mm thick, and the area of overlap was $4 \times 4 \text{ cm}^2$. The veto counter measured $15 \times 15 \text{ cm}^2$, was 1 cm thick and had a circular hole with a 2-cm diameter in its center. A coincidence between the logic signals from $T1$ and $T2$, combined with the *absence* of a signal in the veto counter provided the trigger. The trajectories of individual beam particles could be reconstructed with the information provided by two small drift chambers ($DC1$, $DC2$) which were installed on either side of the trigger counter system. These drift chambers made it possible to determine the location of the impact point of the beam particles at the calorimeter with a precision of typically $\sim 0.5 \text{ mm}$.

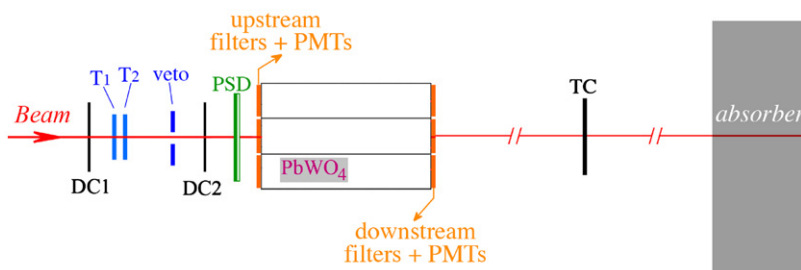


Fig. 6. Experimental setup in which the PbWO_4 crystal matrix was tested (not to scale). See text for details.

The contamination of the beam by non-electrons was typically at the level of a few % or less, except for tertiary beams with momenta close to the secondary particle momentum. We used three additional counters to recognize and eliminate this contamination event-by-event:

- A *preshower detector* (PSD) installed less than 50 cm upstream of the calorimeter. This device consisted of 5 mm of lead, backed up by a plastic scintillator. Muons and pions typically produced a mip signal in this detector, while electrons started to shower in the lead and produced a larger signal.
- About 4 m behind the crystal calorimeter, a *tail catcher* (TC) was installed. This $20 \times 20 \text{ cm}^2$ scintillator paddle was very effective in recognizing contaminating hadrons, which would produce large signals in it. Electron showers were in practice almost fully contained in the crystal matrix, and most of the shower particles that did escape did so at angles larger than a few degrees, so that they physically missed the TC.
- About 20 m downstream, behind more than 10 nuclear interaction lengths of absorber material, a *muon counter* (μ) was installed. This $50 \times 50 \text{ cm}^2$ scintillator paddle was very effective in recognizing contaminating muons, especially at high energies.

In some of the tests described in this paper, the experimental setup was somewhat different from the one depicted in Fig. 6. For example, when the BGO matrix was tested, the PSD (see Fig. 6) was replaced by an interaction target.⁵ In addition, the original DREAM fiber calorimeter was installed directly behind the crystal matrix. This setup offered the additional possibility to study the performance for hadronic showers [15].

2.3. Data acquisition

Measurements of the time structure of the crystal signals formed a very important part of the tests described here. In order to limit distortion of this structure as much as possible, we used special 15 mm thick low-loss cables to transport the crystal signals to the counting room. Such cables were also used for the signals from the trigger counters, and these were routed such as to minimize delays in the DAQ system.⁶ Other signals, e.g. from the muon counter and the Tail Catcher, were transported through RG-58 cables with (for timing purposes) appropriate lengths to the counting room.

The data acquisition system used VME electronics. A single VME crate hosted all the needed readout and control boards. The signals from the auxiliary detectors (PSD, TC and muon counter) were integrated and digitized with a sensitivity of 100 fC/count

⁵ The interaction target consisted of 10 cm of plastic, followed by a scintillator paddle. It represented 0.3 radiation lengths or 0.15 nuclear interaction lengths. High-multiplicity nuclear interactions in this target were used to mimic jets.

⁶ We measured the signal speed to be 0.78c in these cables.

and a 12-bit dynamic range on a 32-channel CAEN V862AC module. The timing information of the tracking chambers was recorded with 1 ns resolution in a 16-channel CAEN V775NC TDC.

The time structure of the calorimeter signals was recorded by means of a digitizer based on the DRS-IV chip [16]. This chip offers both a very fast sampling rate and a wide buffer. It works as follows. The input signal is stored in an array of 1024 switch capacitors. A GHz “domino” wave travels in a circular fashion through a chain of inverters. The wave is stopped by the trigger signal, which “freezes” the charge in the sampling capacitors. The charge pattern is then read out by a shift register and digitized outside the chip. This device makes it possible to measure the time structure of the signals with excellent resolution over a relatively large time window (from 1 μs to 200 ns for a sampling frequency of 1–5 Gs/s).

We used a 32-channel CAEN V1742 VME unit, which is based on the DRS-IV chip, for our purpose [17]. The sampling frequency was set at 2.5 Gs/s (BGO) or 5 Gs/s (PbWO_4), which gave us for every signal 1024 data points, separated by 0.4 or 0.2 ns, respectively. Our readout scheme optimised the CPU utilization and the data taking efficiency thanks to the bunch structure of the SPS cycle, where beam particles were provided to our experiment during a spill of 9.6 s, with a repetition period of 48 s. During the spill the data were saved in a temporary buffer. Between spills, the content of that buffer was copied to the disk. We were able to reach, in spill, a data acquisition rate of $\sim 2 \text{ kHz}$, limited by the speed of the readout electronics. No zero suppression was implemented, so that the event size was constant: $\sim 1.5 \text{ MB}$, largely dominated by the DRS data. An example of the quality of the information obtained in this way is illustrated in Fig. 15.

2.4. Experimental data and analysis methods

Experimental data were taken with electron beams at energies of 4, 6, 10, 15, 20, 30, 40, 50, 60, 80, 100, 120, 150 and 180 GeV. With the exception of 180 GeV, all beams were of the “tertiary” type (see Section 2.2). They were derived from secondary beams at 180 GeV (30–150 GeV tertiaries) or 60 GeV (4–50 GeV tertiaries).

The electron beams were steered into the center of the matrix under study. For each energy, typically 50,000 events were collected, with the exception of the lowest energies, where the event rate was very low. In addition, 5000 randomly triggered events provided pedestal information.

For each event, the full time structure of the signals from each PMT was recorded, i.e. the 16 PMTs reading out the light produced in the BGO matrix, or the 14 PMTs connected to the upstream and downstream end faces of the seven PbWO_4 crystals. In addition, the ADC and TDC data from the auxiliary detectors (wire chambers, trigger counters, and muon counters) were recorded as well.

Off-line, the beam chamber information was used to select events that entered the crystal in a small (typically $10 \times 10 \text{ mm}^2$)

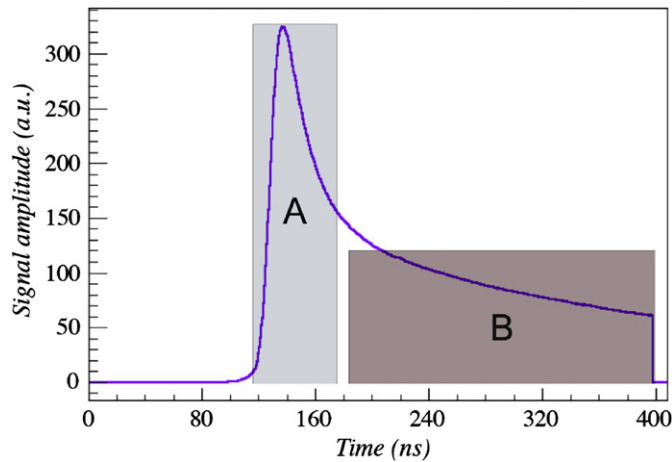


Fig. 7. Average waveform for 100 GeV electrons in the BGO crystal matrix, equipped with UG11 filters. The DRS sampling frequency was 2.5 GHz. The data measured in areas A and B were used to decompose the signals into Čerenkov and scintillation components, as described in the text.

region located around its geometric center. The electron beams contained small fractions (typically $< 1\%$, except near the boundaries of the energy range) of muons (mainly at low energies) and hadrons (mainly at high energies). These were efficiently eliminated with the information from the auxiliary detectors (PSD, TC, muon counter, see Section 2.2). Typically, more than half of the recorded events survived these cuts, except at the lowest energy (20 GeV), where the beam spot was large and the (muon) contamination substantial.

The time structure information of the signals was used to determine their scintillation and Čerenkov components. For each component, the integrated charge was determined from the waveform. This integrated charge was then converted into deposited energy using the calibration constants (see Section 2.5). Fig. 7 shows an average waveform for the signals from the BGO matrix, which clearly shows the contributions of the Čerenkov and scintillation light generated in the electron shower. In order to determine the amounts of light contained in these two components, the waveform for each event was integrated over two gates: A, from 100 to 180 ns; B, from 180 to 400 ns. From studies of pure scintillation waveforms, obtained with a yellow filter, we deduced that the total amount of scintillation light was 36% larger than that obtained in gate B. This information made it possible to determine both the total amount of scintillation light ($S = 1.36 \times Q_B$) and the amount of Čerenkov light ($C = Q_A - 0.36 \times Q_B$) for each individual event. Similar methods were used for the PbWO_4 crystal matrix. Details are given in Section 3.2.

In order to determine the integrated charge, the baseline of the waveform had to be subtracted. This could either be done using the randomly triggered events, or by determining the baseline from the electron signals themselves. The latter method could be used on an event-by-event basis, for example by determining the integrated charge measured in the time interval before the start of the signal (e.g. the interval from 0 to 80 ns in Fig. 7). Both methods were used in these analyses.

2.5. Calibration of the detectors

The PMTs used in these measurements were calibrated with 80 GeV or 30 GeV electron beams. In the case of the PbWO_4 matrix, a narrow beam of electrons (i.e. particles traversing a $10 \times 10 \text{ mm}^2$ region of the upstream drift chambers) was steered into the central regions of each of the seven crystals constituting

the matrix. According to GEANT4-based Monte Carlo simulations [18], which included the experimental information about the beam spread and other cuts that were applied, $\sim 77\%$ of the energy carried by these electrons was deposited in the hit crystal,⁷ while 93% of the energy was deposited in the entire matrix. The latter information formed the basis for the calibration of all 28 signals extracted from this crystal, i.e. the scintillation and Čerenkov signals from the PMTs connected to the upstream and downstream end faces.

After the signals from the crystal placed in the beam line were disentangled into Čerenkov and scintillation components, the integrated charge in each of these components was determined and histograms were made of that integrated charge for all four mentioned signals. Normalization constants c_i were determined to make the average integrated charge in all crystals i equal to that measured in the central crystal. After that, the total integrated charge in the entire matrix could be determined by summing the signals from the seven crystals, multiplied by the proper equalization constant c_i . The average value of that total integrated charge for beam particles traversing the center of the matrix was equated to 93% of the beam energy, and this yielded the conversion factor between the normalized integrated charge and the deposited energy. The calibration constants for the signals from the individual crystals (GeV/pC) followed from that. This procedure was followed for all four mentioned signal types (upstream and downstream scintillation and Čerenkov).

In the case of the BGO matrix, calibration constants had to be assigned to each of the four PMTs that read out the four longitudinal segments of the matrix into which the showers developed. This calibration procedure was carried out in two steps

- First, the gains of all 16 PMTs were equalized, by means of an LED signal with an amplitude comparable to that of a typical electron shower signal. This was done by varying the high voltage at which each individual PMT operated. This procedure was carried out before the PMTs were mounted onto the calorimeter, *without* the UG11 filters. The same LED and the same geometry were used for all 16 PMTs.
- After the PMTs (plus the filters) were mounted on the calorimeter, 100 GeV electrons were sent into each of the four columns (see Fig. 1) and the HV values of the four PMTs in the hit column were varied, in an iterative procedure, until the energy resolution for the summed signals reached a minimum value. Because of the size of this calorimeter, shower leakage was negligible and we assumed that the integrated charge collected by the 16 PMTs was a good measure of the deposited energy (100 GeV). On that basis, the integrated charge measured in each individual PMT contributing to the signal could be converted into GeV as well. We checked this procedure using measurements in which the beam spot was moved horizontally across columns 2 and 3 (see Fig. 1) and found the response to be constant.

3. Experimental results

3.1. Results for the BGO matrix

Experimental data were taken with electron beams of 30, 60, 100 and 150 GeV. Fig. 8 shows typical distributions of the integrated charge for scintillation and Čerenkov light, measured for 100 GeV electrons showering in the BGO matrix. The energy

⁷ The Monte Carlo simulations showed a small difference ($+0.2\%$) between the energy deposited in the central crystal and the six other crystals, because of the effects of inward scattering from the surrounding environment.

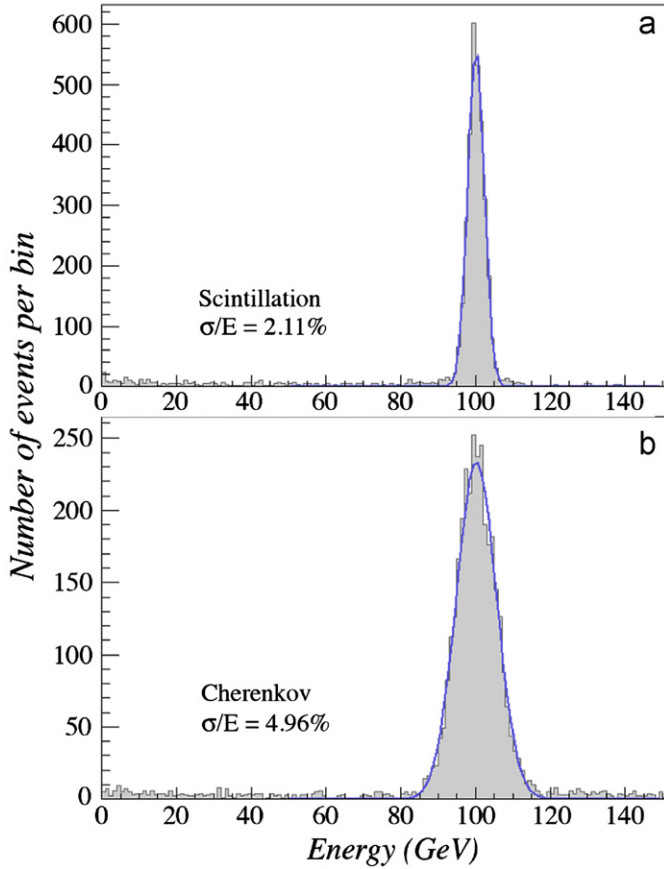


Fig. 8. Signal distributions for 100 GeV electrons in the BGO matrix, for the scintillation (a) and Cherenkov (b) components, respectively. Also shown are the results of Gaussian fits to these distributions.

resolution, derived from Gaussian fits to these distributions, is 2.11% and 4.96%, respectively.

The energy resolution is shown as a function of energy in Fig. 9. The horizontal axis is drawn linear in $E^{-1/2}$. Therefore, if the energy resolution would only be affected by stochastic (Poissonian) fluctuations, the experimental points would be located on a straight line through the bottom right corner of the plot. The figure shows the results of fits of the type $\sigma/E = aE^{-1/2} + b$. It turns out that the resolution obtained for the scintillation component, as well as that for the total collected charge (i.e. the integral over the entire waveform shown in Fig. 7), are well described by $E^{-1/2}$ scaling ($b \approx 0$). On the other hand, the energy resolution measured for the Cherenkov component exhibits a deviation, with $b \sim 1.5\%$. Apparently, the resolution for this component is affected by significant non-Poissonian fluctuations.

The resolutions shown here are of course much worse than those typically obtained with BGO calorimeters [9]. However, one should keep in mind that in order to operate this crystal as a dual-readout calorimeter, we selected a small fraction of 1% of the light produced in the crystals, in a wavelength range in which that light is strongly attenuated, and read it out in a very awkward geometry.

We also investigated the linearity of the observed signals in the BGO matrix. The results are shown in Fig. 10. In Fig. 10a, the average signal is plotted as a function of the electron energy. Results are given for the total integrated charge, and for the integrated charge contained in the Cherenkov and scintillation components, as defined in Section 2.4 (i.e. C and Q_B , respectively). The data points are well described by straight lines through the origin, which are shown as well in Fig. 10a. The fractional

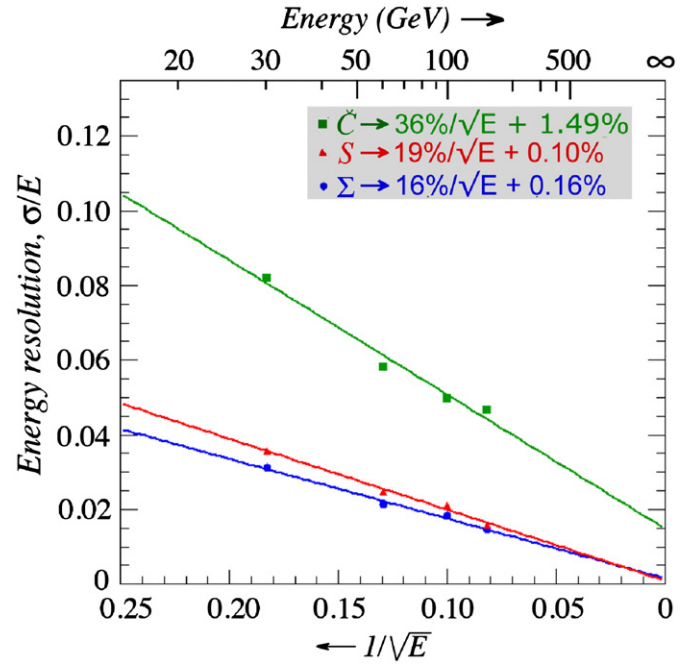


Fig. 9. The energy resolution for electrons in the BGO matrix, as a function of the energy of the showering particles. Results are given for the total charge collected by the PMTs (Σ), and for the Cherenkov (C) and scintillation (S) components of the signal. Also shown are the results of fits of the type $\sigma/E = aE^{-1/2} + b$ to the experimental data points.

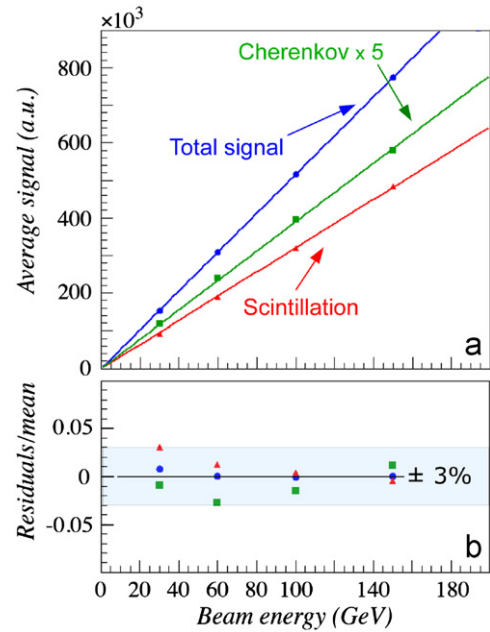


Fig. 10. Linearity of the BGO matrix for electron detection. Shown are the average total integrated signal, as well as the Cherenkov and scintillation components of that signal, as a function of energy. The results of linear fits through these data points, and the fractional residuals of these fits, are shown as well.

residuals from these fits, shown in Fig. 10b, indicate that the calorimeter is reasonably linear for both light components, at least in the energy range covered by these measurements.

3.2. Results for the $PbWO_4$ matrix

In the first series of measurements carried out with the molybdenum-doped $PbWO_4$ matrix, the light generated by

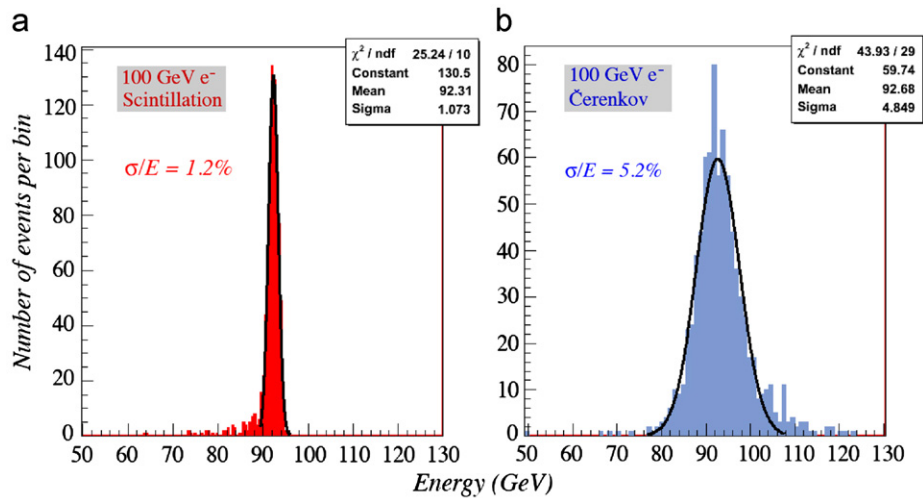


Fig. 11. Signal distributions for 100 GeV electrons detected in the PbWO₄ crystal matrix, for the scintillation and Čerenkov components of the signals. Also shown are the results of Gaussian fits to these distributions. The scintillation signals were obtained using the light filtered through a GG495 filter mounted at the upstream end, the Čerenkov signals were obtained using the light filtered with a U330 filter mounted at the downstream end of the crystal matrix. See text for details.

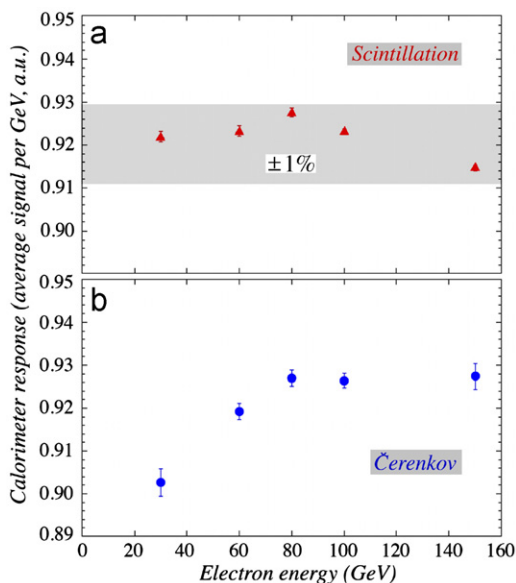


Fig. 12. Signal linearity for electrons detected in the Mo-doped PbWO₄ crystal matrix. Shown are the response, i.e. the average signals per GeV deposited energy, as a function of the electron energy for the scintillation signals (a) and the Čerenkov signals (b). The matrix was equipped with a GG495 filter at the upstream end, and a U330 filter downstream.

electron showers was filtered with a U330 filter mounted at the downstream end face, and a GG495 filter at the upstream one. The resulting signals consisted for $\sim 80\%$ of Čerenkov light downstream, and for $> 99\%$ of scintillation light at the upstream end of the crystal matrix.

Data were taken in this configurations for electrons beams at energies of 30, 60, 80, 100 and 150 GeV. Integrated-charge distributions measured for 100 GeV electrons at the upstream and downstream ends of the crystal matrix are shown in Fig. 11a and b, respectively. Whereas the scintillation component of the shower signals was detected with a resolution of about 1%, as might be expected in a calorimeter of this type, the precision with which the Čerenkov component was measured was quite poor.

Measurements at other energies revealed one factor that contributed to this rather mediocre performance. Fig. 12 shows the calorimeter response, i.e. the average signal per unit

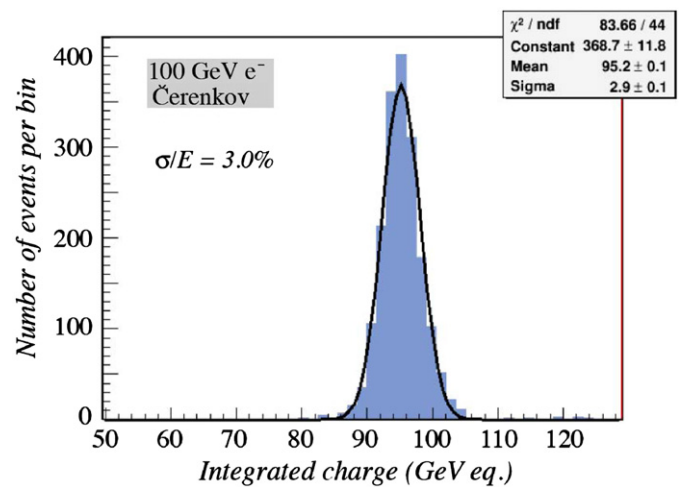


Fig. 13. The Čerenkov signal distributions for 100 GeV electrons detected in the Mo-doped PbWO₄ crystal matrix. The upstream and downstream end faces of the calorimeter were both equipped with a U330 filter. The Čerenkov signals detected on both ends were summed.

deposited energy, as a function of energy, separately for the scintillation (Fig. 12a) and Čerenkov (Fig. 12b) components. While the matrix turned out to be extremely linear for the detection of the scintillation light (the highlighted area in Fig. 12a represents response variations of $\pm 1\%$ about the average), the response to the Čerenkov light clearly increases with the shower energy. This effect is most likely the result of attenuation of the predominantly ultraviolet light transmitted by the U330 filter. As the shower energy increases, the light is produced deeper inside the crystals, i.e. closer to the downstream end face where the Čerenkov light detection takes place, hence less attenuated.

The result is a 3% larger response at 100 GeV than at 30 GeV. Based on parameterized longitudinal shower profiles, we estimate that the average depth at which the light is produced increases by $\sim 2X_0$ when the energy is increased from 30 to 150 GeV. Since this depth fluctuates on a scale of $1X_0$ in individual showers induced by electrons of a given energy, we estimate that these fluctuations alone contribute 1–2% to the energy resolution.

In order to reduce this effect, we equipped both the upstream and downstream end faces of the matrix with filters that would

enhance the Čerenkov component of the detected signals. It is well known that reading out a device in which light is strongly attenuated from both ends and adding the signals greatly reduces the attenuation effects on the total signals.

The effect of adding the upstream and downstream Čerenkov signals is illustrated in Fig. 13 for 100 GeV electrons. The energy resolution of 3% represents indeed a considerable improvement with respect to the measurements in which the Čerenkov signal was determined from the downstream PMT alone. This improvement is, apart from a reduction of the attenuation effects, of course also due to the increased number of photoelectrons contributing to the signals.

Also the signal linearity benefitted from combining the upstream and downstream Čerenkov signals. Fig. 14 clearly

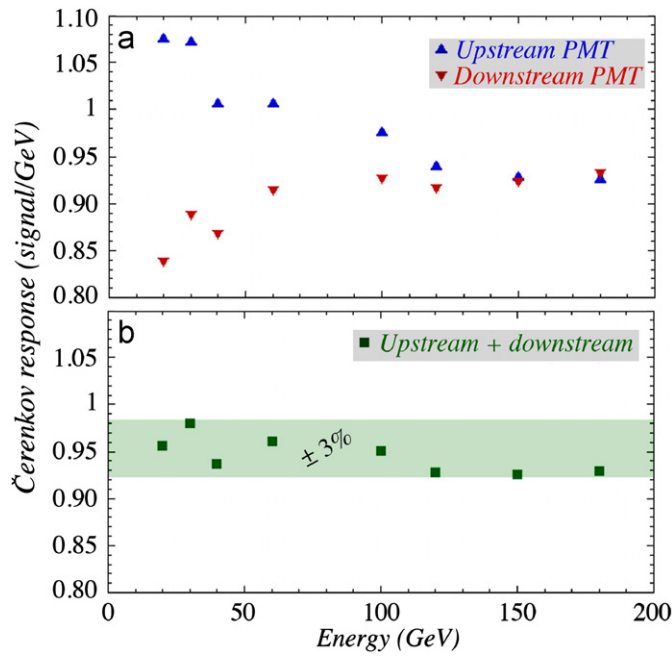


Fig. 14. Signal linearity for electrons detected in the Mo-doped PbWO₄ crystal matrix. Shown is the response as a function of the electron energy for the Čerenkov signals. The matrix was equipped with U330 filters, both at the upstream and downstream end faces. The signals measured at both ends are both shown separately (a) and added together (b).

illustrates the effects discussed above. As the shower energy increased, the light was produced, on average, deeper inside the crystals. As a result of the attenuation of the short-wavelength Čerenkov light, the response of the upstream PMT decreased, while the response of the downstream PMT increased (Fig. 14a). When these signals were summed together, the detector turned out to be reasonably linear, the response is constant to within a few percent (Fig. 14b).

The main disadvantage of this readout geometry is that the U330 filters transmit almost no scintillation light. In an alternative setup, we therefore replaced the downstream U330 filter by a UG5 one, which also transmits light with wavelengths in the region around 500 nm, where scintillation dominates (see Fig. 5a). This led to a usable scintillation signal.

Fig. 15 shows the average time structure of the signals from 30 GeV electrons measured with these two types of filters, both on a linear and an (inverted) logarithmic scale. The scintillation component is visible as a tail in the UG5 pulses, which is largely

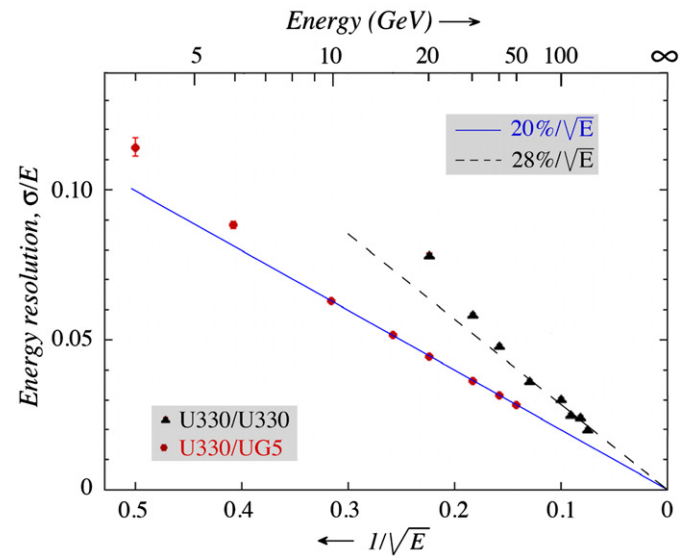


Fig. 16. Energy resolution for electrons showering in the PbWO₄ crystal matrix, as a function of energy. The data points concern the resolution measured for the Čerenkov signals, derived from UV-filtered light detected at both ends of the crystal matrix. See text for details.

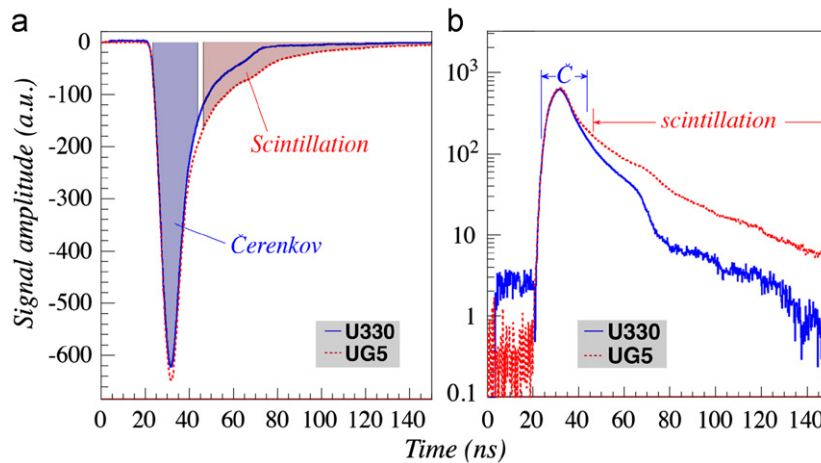


Fig. 15. The average time structure of 30 GeV electron signals measured in the PbWO₄ crystal matrix equipped with a U330 filter or a UG5 filter. The latter transmits also a significant fraction of the scintillation light. Light collected in a time window of 20 ns around the peak is considered Čerenkov light, light collected more than 15 ns beyond the peak is considered scintillation light. The corresponding gates are indicated in the figure, which shows the time structure on a linear (a) and an inverted logarithmic scale (b).

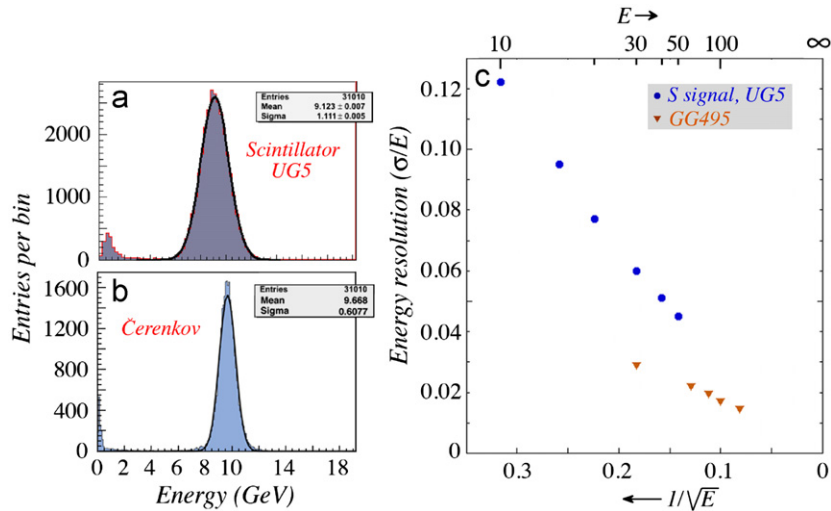


Fig. 17. Signal distributions for the scintillation (a) and Čerenkov (b) components of the light generated in the PbWO_4 matrix by 10 GeV electron showers and filtered with the U330/UG5 combination. The energy resolution of the scintillation signal is compared with that obtained with the yellow (GG495) filter in diagram (c).

absent in the U330 ones. The Čerenkov light is predominantly concentrated in a narrow window around the peak. In our analyses, a 20 ns width was used for this window, as indicated in Fig. 15. For the scintillation light, the tail of the UG5 pulses was used.

Measurements in which the Čerenkov signal was determined from a combination of upstream and downstream signals were carried out for a large number of electron energies, ranging from 4 to 180 GeV. Initially, measurements with the U330/U330 filter combination were carried out for tertiary electrons of 20–150 GeV, derived from a 180 GeV secondary beam, as well as for 180 GeV secondary electrons. Later, measurements in the low energy range (4–50 GeV tertiary electrons derived from a 60 GeV secondary beam) were performed with the UG5/U330 filter combination.

The energy resolution obtained for the Čerenkov channel is shown as a function of the electron energy in Fig. 16 for these two sets of experimental data. Each data set is reasonably well described by a straight line through the bottom right corner in this plot. These lines, drawn to guide the eye, indicate that stochastic fluctuations are indeed a dominating component of the energy resolution.

The resolutions measured at the low-energy end of each data set deviate from the straight lines. These deviations are consistent with the contribution of the signal baseline fluctuations to the measured energy resolution. We measured this contribution for the sum of the 14 signals considered here from the signal distributions obtained with random triggers, and found it to be equivalent to 215 MeV/E for the U330/UG5 measurements, and 480 MeV/E for the U330/U330 measurements, respectively. The stochastic fluctuations that dominate the measured energy resolutions were found to contribute $20\%/\sqrt{E}$ and $28\%/\sqrt{E}$ for these two data sets. Unlike in the BGO matrix, no evidence was found for an energy independent contribution (“constant term”) to the energy resolution.

The UG5 filter transmitted a larger fraction of the Čerenkov light than the U330 filter, and thus led to larger signals, and a correspondingly smaller relative contribution of signal baseline fluctuations to the energy resolution. The fact that the energy resolution measured for the Čerenkov component improved when one of the U330 filters was replaced by a UG5 one also strongly indicates that the resolution is dominated by (fluctuations in) the Čerenkov light yield. Taking the slope of the lines in Fig. 16 at face value, we find this light yield to be 25 Čerenkov photoelectrons (C.p.e.) per GeV ($\sigma/E = 20\%/\sqrt{E}$, U330/UG5) or 13 C.p.e./GeV ($\sigma/E = 28\%/\sqrt{E}$, U330/U330).

Even though the UG5 filter led to usable scintillation signals, the energy resolution for electron showers measured in the scintillation channel was somewhat worse than in the Čerenkov channel, and about a factor of two worse compared to resolutions measured with the yellow (GG495) filter. This is of course due to the very small fraction of the scintillation light that was detected in this setup. Fig. 17 shows typical scintillation and Čerenkov signal distributions for 10 GeV electrons obtained with the U330/UG5 filter combination (Fig. 17a and b), as well as a comparison between the energy resolution for the scintillation signals as a function of energy, obtained with the UG5 and GG495 filters (Fig. 17c).

4. Discussion

Our interest in studying high-Z scintillating crystals for the purpose of dual-readout calorimetry derived from the potential reduction of the contribution of stochastic fluctuations to the energy resolution of such calorimeters. In the fiber calorimeter with which the benefits of dual-readout calorimetry were first demonstrated [1], the contribution of such fluctuations was $\sim 40\%/\sqrt{E}$, with approximately equal contributions ($\sim 30\%/\sqrt{E}$) from sampling fluctuations and from Čerenkov photoelectron statistics. Our goal in further developing this experimental technique is to reduce the contribution of stochastic fluctuations to the point where these are comparable to the irreducible effects of fluctuations in visible energy, estimated at $\sim 15\%/\sqrt{E}$ [19]. Crystals were believed to offer good opportunities in this respect.

However, as the results of this study show, things are not so easy. Extracting sufficiently pure Čerenkov signals from these scintillating crystals implies a rather severe restriction to short wavelengths. As a consequence,

- a large fraction of the potentially available Čerenkov photons needs to be sacrificed, but also,
- the light that does contribute to the Čerenkov signals is strongly attenuated, because of the absorption characteristics of the crystals.

As an aside, we mention that these characteristics also make crystal-based dual-readout calorimeters probably quite prone to radiation damage.

Our results show that the stochastic fluctuations in the Čerenkov channel are at best $20\%/\sqrt{E}$ in the case of our

Mo-doped PbWO_4 crystal matrix. Assuming that these fluctuations are completely determined by photoelectron statistics, this would mean that the Čerenkov light yield for the electron showers was 25 photoelectrons per GeV deposited energy. In a previous study with a single crystal of this type, we measured this light yield to be 55 C.p.e./GeV [5]. This difference is most certainly due to the fact that the latter measurement concerned particles traversing the crystal at the Čerenkov angle, thus maximizing the light yield. The light yield now observed for showers is consistent with the results obtained for the angular dependence of the signals in the single crystal.

A similar difference was found for the BGO matrix. From measurements with beam particles traversing a single BGO crystal, the Čerenkov light yield was determined to be ~ 30 C.p.e./GeV [3], while the results shown in Fig. 9 suggest a light yield that is about a factor of five less. The fact that this difference is even larger than in the case of PbWO_4 (c.f. also the difference between the magnitude of the Čerenkov peaks in Figs. 3 and 7) may be due to the thicker (UV absorbing!) glass windows used in the detection of the shower signals, plus the fact that the BGO crystals were only read out on one side.

In any case, using crystals in combination with filters does not seem to offer a benefit in terms of the Čerenkov light yield in dual-readout calorimeters. Since crystals are not effective either in detecting the numerous evaporation neutrons whose energy is correlated with the invisible energy, the irreducible resolution limit is also higher in crystal-based calorimeters, compared to devices in which plastic (i.e. hydrogenous) fibers provide the signals. For these reasons, the fiber option has now a higher priority in the RD52 project.

Acknowledgments

We thank CERN for making its facilities available for our experiments. This study was carried out with financial support

of the United States Department of Energy, under contract DE-FG02-07ER41495, and by Italy's Istituto Nazionale di Fisica Nucleare.

References

- [1] N. Akchurin, et al., Nuclear Instruments and Methods in Physics Research Section A 537 (2005) 537.
- [2] N. Akchurin, et al., Nuclear Instruments and Methods in Physics Research Section A 582 (2007) 474.
- [3] N. Akchurin, et al., Nuclear Instruments and Methods in Physics Research Section A 595 (2008) 359.
- [4] N. Akchurin, et al., Nuclear Instruments and Methods in Physics Research Section A 604 (2009) 512.
- [5] N. Akchurin, et al., Nuclear Instruments and Methods in Physics Research Section A 621 (2010) 212.
- [6] <http://sba.web.cern.ch/sba/BeamsAndAreas/resultbeam.asp?beamline=H8>.
- [7] N. Akchurin, et al., Nuclear Instruments and Methods in Physics Research Section A 638 (2011) 47.
- [8] N. Akchurin, et al., Nuclear Instruments and Methods in Physics Research Section A 640 (2011) 91.
- [9] B. Adeva, et al., Nuclear Instruments and Methods in Physics Research Section A 289 (1990) 35.
- [10] B. Lewandowski, Nuclear Instruments and Methods in Physics Research Section A 494 (2002) 303.
- [11] K. Miyabayashi, Nuclear Instruments and Methods in Physics Research Section A 494 (2002) 298.
- [12] CMS Collaboration, Journal of Instrumentation 5 (2010) T03011.
- [13] N. Akchurin, et al., Nuclear Instruments and Methods in Physics Research Section A 550 (2005) 185.
- [14] I.M. Frank, I.E. Tamm, Doklady Akademi Nauk SSSR 14 (1937) 107.
- [15] N. Akchurin, et al., Nuclear Instruments and Methods in Physics Research Section A 610 (2009) 488.
- [16] S. Ritt, et al., Nuclear Instruments and Methods in Physics Research Section A 623 (2010) 486.
- [17] For a detailed description of this module, see <http://www.caen.it/csite/CaenProd.jsp?idmod=661&parent=11>.
- [18] S. Agostinelli, et al., Nuclear Instruments and Methods in Physics Research Section A 506 (2003) 250.
- [19] R. Wigmans, Calorimetry-energy Measurement in Particle Physics, International Series of Monographs on Physics, vol. 107, Oxford University Press, 2000, p. 256ff (references therein).